



Insight into the dual-channel charge-carrier transfer path for nonmetal plasmonic tungsten oxide based composites with boosted photocatalytic activity under full-spectrum light

Yaocheng Deng^{a,b}, Lin Tang^{a,b,*}, Chengyang Feng^{a,b}, Guangming Zeng^{a,b,*}, Zhaoming Chen^{a,b}, Jiajia Wang^{a,b}, Haopeng Feng^{a,b}, Bo Peng^{a,b}, Yani Liu^{a,b}, Yaoyu Zhou^c

^a College of Environmental Science and Engineering, Hunan University, Changsha, 410082, China

^b Key Laboratory of Environmental Biology and Pollution Control, Hunan University, Ministry of Education, Changsha, 410082, China

^c College of Resources and Environment, Hunan Agricultural University, Changsha, 410128, China

ARTICLE INFO

Keywords:

Tungsten oxide
Nonmetal plasmonic semiconductors
Z-scheme
Dual-channel process
Oxygen vacancies

ABSTRACT

The photocatalytic activities of the semiconductor-based photocatalysts are often practically limited by the insufficient photoinduced charge-carrier separation, so the construction of efficient charge transfer path is vital for highly efficient photocatalysis reaction system. In this study, we reported a rational designed novel hierarchical $W_{18}O_{49}/g-C_3N_4$ composite with boosted photocatalytic activity through the manipulated flow of dual-channel charge-carrier separation and transfer process. Due to the efficient strategy about the combination of the morphology structure and the regulation of band structure, the prepared composites present enhanced photocatalytic performance in both full-spectrum light and near-infrared (NIR) light irradiation. Under the optimum condition, the prepared $W_{18}O_{49}/g-C_3N_4$ composites show high degradation efficiency for both colorful methylene blue (MB) and colorless ciprofloxacin (CIP). Mechanistic characterizations and control experiments demonstrate the cooperative synergy effect of dual-channel charge-carrier transfer path in such $W_{18}O_{49}/g-C_3N_4$ composites, including Z-scheme charge transfer and surface plasmon resonance effect, which interactively leads to the boosted photocatalytic performance. The match of the band gap results in the Z-scheme reaction mechanism and brought both the strong redox ability and promotion of the transfer rate of the photogenerated charges; the LSPR effect of nonmetal plasmonic $W_{18}O_{49}$ can broaden the light response of the prepared $W_{18}O_{49}/g-C_3N_4$ to NIR region, leading to enhanced utilization of solar energy. Moreover, the oxygen vacancies in this reaction system which played important role in the photocatalytic process have been fully studied by the appropriate design of the control experiments.

1. Introduction

Photocatalysis technology based on semiconductor materials aiming at solving the global environmental pollution and energy crisis has become one of the most promising avenues in the worldwide [1–4]. Thus, various high-efficient and environmental-friendly photocatalysts have been designed and employed [5–9]. However, the photocatalytic activity of most single-component photocatalysts is still far from satisfactory due to the fast recombination efficiency of the photoinduced charge carriers, which inhibits the migration of these charges to reach the semiconductor surface to participate in the redox reactions [10,11]. To solve this dilemma, various approaches have been explored to promote the transfer rate of the photogenerated charge-carrier.

Rational construction of heterostructure with band matchable

semiconductors is commonly regarded as an efficient way to impede the recombination of the charge-carrier by space separation of photo-generated holes and electrons [12,13]. But traditional heterojunctions would reduce the redox ability of photogenerated charges due to the ineluctable charge transfer process from high band level to relative low band level. On the contrary, new types of Z-scheme photocatalysts can effectively avoid the above problems, retaining the strong redox ability of the photogenerated charges with improved photocatalytic activity [14,15]. Therefore, designing new Z-scheme photocatalysts via the proper combination of different semiconductors is fascinating. Additionally, the use of local surface plasmon resonance (LSPR) would be another efficient strategy to promote the charge transfer in the composite, and many researchers prefer it [16–18]. However, to maximize the charge transfer rate and separation efficiency, promotion strategy

* Corresponding authors at: College of Environmental Science and Engineering, Hunan University, Changsha, 410082, China.

E-mail addresses: tanglin@hnu.edu.cn (L. Tang), zgming@hnu.edu.cn (G. Zeng).

<https://doi.org/10.1016/j.apcatb.2018.04.075>

Received 25 January 2018; Received in revised form 22 April 2018; Accepted 29 April 2018

Available online 30 April 2018

0926-3373/ © 2018 Elsevier B.V. All rights reserved.

just via only one charge-carrier transfer channel is difficult to achieve the goal. Therefore, it is important to optimally integrate different charge separation strategy in a well-designed hybrid photocatalysts to synergistically improve the photocatalytic performance.

Graphitic carbon nitride ($g\text{-C}_3\text{N}_4$), a stable and nontoxic polymeric semiconductor, has attracted great attentions as a visible-light excited photocatalysts for photocatalytic degradation [19–24]. Tremendous interests have focused on the combination of $g\text{-C}_3\text{N}_4$ with inorganic semiconductors, especially for the construction of Z-scheme reaction mechanism, to achieve spatial separation of charge carriers and improve photocatalytic performance [25–27]. Unfortunately, due to that the intrinsic strong coulomb interactions of single Frenkel excitons in $g\text{-C}_3\text{N}_4$ resulted in sluggish exciton dissociation, the photocatalytic performance of these $g\text{-C}_3\text{N}_4$ based photocatalysts needs to be further improved [28–30].

In addition, grafting plasmonic metal to semiconductors to employ the local surface plasmon resonance (LSPR) effect would be another efficient strategy to boost the charge-carrier separation of photocatalysts [31]. In the past decade, some conducting metals, such as Au, Ag and Pt have been applied into the photocatalysis process to obtain enhanced photocatalytic performance based on the LSPR effect [32,33]. The existence of these metals provides a unique pathway for solar harvesting, and the LSPR effect can broaden the light response range and promote the photogenerated charge transfer rate. However, the high-cost of noble metals limits their large-scale practical applications. Recently, new types of nonmetal semiconductors have been investigated, such as WO_{3-x} , [32] Cu_{2-x}S , [34] MoO_{3-x} , [35] and Sn-doped In_2O_3 , [36]. These semiconductors also have LSPR effect due to the existence of element vacancies. The free charges on the surface of the vacancy-rich nanoparticles can be induced by the incident and cause collective oscillation, giving opportunities to design new kind of low-cost and noble-metal-free plasmonic semiconductor materials. Nevertheless, owing to the low density of free charges, the LSPR absorption of those nonmetal nanoparticles usually locates in the NIR region, which indicates that the combination with another proper semiconductor is necessary to obtain high photocatalytic performance. Among these nonmetal semiconductors, $\text{W}_{18}\text{O}_{49}$, as member of tungsten oxide, present unique characteristics, showing enhanced performance for photocurrent response and photocatalytic water oxidization due to its LSPR effect [28,37]. It has been demonstrated that the existence of oxygen vacancies on $\text{W}_{18}\text{O}_{49}$ surfaces bring about the plasmon-driven activities under visible light and NIR light irradiation [38,39]. Some researchers have found that the LSPR effect can improve the photocatalytic activity of plasmonic tungsten oxides ($\text{W}_{18}\text{O}_{49}$) in the full spectrum (UV–vis–NIR) region, and the oxygen vacancies can also serve as the reaction sites to improve the reaction process [32,40,41]. Considering the advantages of $g\text{-C}_3\text{N}_4$ and $\text{W}_{18}\text{O}_{49}$, and combined with the investigations of the interfacial charge density migration and charge carrier effective masses, it is revealed that dual-channel charge-carrier transfer path would be established. One channel would be the direct Z-scheme electron transfer process between $\text{W}_{18}\text{O}_{49}$ and $g\text{-C}_3\text{N}_4$. Another channel would be the LSPR effect caused by nonmetal plasmonic $\text{W}_{18}\text{O}_{49}$ from its oxygen vacancies. The rapid electron transfer between $\text{W}_{18}\text{O}_{49}$ and $g\text{-C}_3\text{N}_4$ via the dual-channel charge transfer path would result in both slower recombination rate and prolonged lifetime of photogenerated charge carriers than that in the single component.

Thus, in this study, novel $\text{W}_{18}\text{O}_{49}/g\text{-C}_3\text{N}_4$ nanograin composites with superior full-spectrum-light response ability have been synthesized successfully via facial hydrothermal supported self-assembly process. Benefit from the designed unique structure and match of the band gap, the photogenerated charges transfer of the prepared $\text{W}_{18}\text{O}_{49}/g\text{-C}_3\text{N}_4$ nanograin composites have been greatly improved via dual-channel transfer path: Z-scheme charge transfer and surface plasmon resonance effect. Thus, the prepared $\text{W}_{18}\text{O}_{49}/g\text{-C}_3\text{N}_4$ nanograin composites present enhanced photocatalytic degradation efficiency for both colored methylene blue (MB) and colorless ciprofloxacin (CIP).

Additionally, the role of oxygen vacancies in this reaction process have been fully investigated, and results show that due to the existence of LSPR effect, the hot-electrons can be injected into the conduction band of $g\text{-C}_3\text{N}_4$, and contribute to the enhanced photocatalytic performance. The reported highly efficient photocatalyst with unique charge transfer process provides a new insight into the design of photocatalyst.

2. Experimental section

2.1. Materials

Hexacarbonyltungsten ($\text{W}(\text{CO})_6$) and Ciprofloxacin (CIP) were purchased from Aladdin Industrial Corporation. Melamine, absolute ethanol, Isopropanol (IPA), Ethylenediaminetetraacetic acid disodium (EDTA-2Na) and 1,4-benzoquinone (BQ) was purchased from Sinopharm Chemical Reagent Co., Ltd. Other reagents were of analytical grade and used as received without further purification. All solutions were prepared with deionized water (18.25 M Ω cm specific resistance), which was produced by an Ultrapure laboratory water system.

2.2. Preparation of the $\text{W}_{18}\text{O}_{49}/g\text{-C}_3\text{N}_4$ photocatalysts

First of all, the graphitic nitride ($g\text{-C}_3\text{N}_4$) nanosheets were synthesized via a thermal polymerization method. Typically, 5 g of melamine was placed into an alumina crucible and covered to create semiclosed reaction environment. Subsequently, the alumina crucible was heated to 520 °C with a rising rate of 5 °C/min and kept at this temperature for 4 h, and then the yellow bulk $g\text{-C}_3\text{N}_4$ can be obtained. To acquire $g\text{-C}_3\text{N}_4$ nanosheets, the bulk $g\text{-C}_3\text{N}_4$ was grinded into powder and placed into the alumina crucible for another thermal process, with the rising rate of 2.5 °C/min to 500 °C and kept for 2 h. Secondly, as for the synthesis of the $\text{W}_{18}\text{O}_{49}/g\text{-C}_3\text{N}_4$ photocatalysts. 50 mg of $\text{W}(\text{CO})_6$ was dissolved in 40 mL of absolute ethanol solution, and then certain amount of the prepared $g\text{-C}_3\text{N}_4$ nanosheets was added into the above solution and stirred for 1 h to obtain the homogeneous mixture. Next, the mixture was sealed in a Teflon-lined autoclave and heated at 160 °C for 12 h. Finally, the yellow-blue precipitates were collected via centrifugation, and washed with ethanol for several time and dried in vacuum. By adjusting the addition dosage of $g\text{-C}_3\text{N}_4$ nanosheets during the hydrothermal process, series of $\text{W}_{18}\text{O}_{49}/g\text{-C}_3\text{N}_4$ photocatalysts can be obtained. For convenience, the added amount of $g\text{-C}_3\text{N}_4$ in the reaction system with 50 mg, 80 mg, 100 mg, 120 mg and 150 mg for the synthesis of the photocatalysts were marked as WCN-1, WCN-2, WCN-3, WCN-4 and WCN-5, respectively. To make comparison, the pure $\text{W}_{18}\text{O}_{49}$ were prepared by using the same route without the addition of $g\text{-C}_3\text{N}_4$ nanosheets.

2.3. Characterization of materials

The Morphology structure of the samples was studied on a Hitachi S-4800 field emission scanning electron microscopy (FE-SEM Hitachi, Japan) with 5.0 kV scanning voltages. Transmission electron microscopy (TEM) and high-resolution transmission electron microscopy were obtained via an F20 S-TWIN electron microscopy (Tecnai G2, FEI Co.) at the acceleration voltage of 200 kV. The crystal structure characteristics of the prepared samples were measured via an X-ray diffractometer (XRD) (Bruker AXS D8 Advances) with Cu K α irradiation source at a scan rate (2 θ) of 0.05 °s^{−1}. FT-IR spectra were obtained on an IRAffinity-1 Fourier transform infrared spectrometer (Shimadzu, Japan) by the standard KBr disk method at room temperature. The X-ray photoelectron spectroscopy (XPS) of the prepared samples was carried out Thermo Fisher ESCALAB 250Xi spectrometer with Al K α source. The Ultraviolet visible near-infrared diffused reflectance spectra (UV–vis–NIR DRS) of the prepared samples were carried out via a UV–vis–NIR spectrophotometer (Hitachi U4100 UV Spectrometer)

equipped with an integrating sphere, using BaSO_4 as the reference. The photoluminescence (PL) measurements were carried out on fluorescence spectrophotometer (FluoroMax-4) at room temperature. The time-resolved transient photoluminescence spectra of the prepared samples were investigated on a FLS980 Series of Fluorescence Spectrometers. The electron spin resonance (ESR) signals of radicals spin-trapped by spin-trapped reagent 5,5-dimethyl-1-pyrroline *N*-oxide (DMPO) were examined on a JES-FA200 spectrometer under visible light irradiation ($\lambda > 420 \text{ nm}$).

2.4. Photocatalytic activity measurement

The photocatalytic activity of the prepared photocatalysts was investigated by the degradation of MB and CIP under light irradiation. A 300 W Xe lamp (PLS/SXE 300 C, Beijing Perfectlight Co., Ltd.) was used as the light source, which was used directly without any filter as the full-spectrum light source, and equipped with a 700 nm filter as the NIR light source. Before the photocatalytic experiments start, 50 mg (100 mg) of the as-prepared photocatalysts was added into 100 mL of 10 mg/L MB (CIP) aqueous solution, and kept stirring in the dark for 30 min to achieve the adsorption equilibrium. During the illumination process, quantitative of aqueous solution was collected at certain time intervals for analysis after centrifugation to removal the photocatalyst. The photocatalytic degradation efficiency was measured using a Shimadzu UV-vis spectrophotometer (UV-2550) at the characteristic absorption peak of 664 nm for MB and 276 nm for CIP.

2.5. Photoelectrochemical measurement

The photoelectrochemical characteristics of the prepared samples was measured by a typical three-electrode measured system based on a CHI 660D workstation, A Pt electrode was used as the counter electrode and an Ag/AgCl electrode in saturated KCl solution was employed as the reference electrode. The measurement of the photocurrent density conducted in a 0.2 M sodium sulfate electrolyte solution under visible light provided by a 300 W Xe arc lamp ($\lambda > 365 \text{ nm}$). Electrochemical impedance spectroscopy (EIS) were measured based on the above photoelectrochemical test system except that the electrolyte was replaced by a 0.1 M KCl solution containing 5 mM $\text{Fe}(\text{CN})_6^{3-/4-}$.

3. Results and discussions

3.1. Structure and morphology characteristics

The crystal structure of the prepared samples was characterized by X-ray diffraction (XRD) measurement, and the results were shown in Fig. 1. As for $\text{g-C}_3\text{N}_4$ nanosheets, two clear diffraction peaks locate at

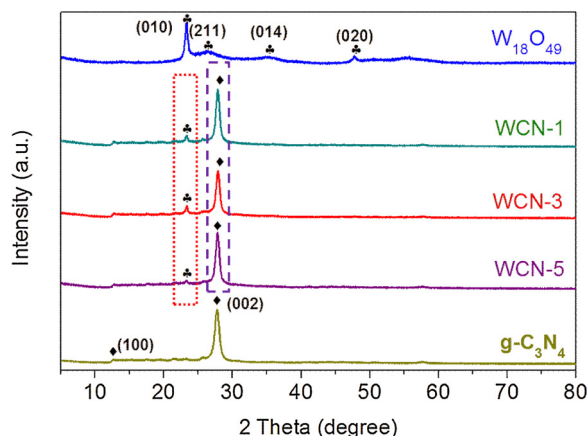


Fig. 1. XRD patterns of the prepared $\text{g-C}_3\text{N}_4$, $\text{W}_{18}\text{O}_{49}$ and WCN-3 samples.

13.2° and 27.4° can be found, representing the in-plane intervals of the periodic tri-s-triazine units as the (100) plane, and the feature inter-planar stacking of aromatic systems as the (002) plane of graphite-like materials, respectively [42]. The diffraction peaks exist on the XRD pattern of $\text{W}_{18}\text{O}_{49}$ can be clearly identified, which belongs to the monoclinic $\text{W}_{18}\text{O}_{49}$ (JCPDS No. 05-0392). The XRD pattern of the prepared $\text{W}_{18}\text{O}_{49}/\text{g-C}_3\text{N}_4$ samples (WCN-1, WCN-3 and WCN-5) possesses the characteristic peaks of both $\text{W}_{18}\text{O}_{49}$ and $\text{g-C}_3\text{N}_4$, indicating the successful combination of $\text{W}_{18}\text{O}_{49}$ and $\text{g-C}_3\text{N}_4$ via the reaction process.

SEM and TEM images were provided to study the morphology of the prepared samples. As shown in Fig. 2a and d, the SEM combines with the TEM image of $\text{g-C}_3\text{N}_4$ confirm its nanosheets structure, from which we can see that the prepared $\text{g-C}_3\text{N}_4$ nanosheets own wrinkled surface, reflecting the layer-stacking of graphite-like conjugated aromatic systems by the weak van der Waals bond. As for pure $\text{W}_{18}\text{O}_{49}$, the peculiar sea urchins structure can be clearly observed, and the $\text{W}_{18}\text{O}_{49}$ sea urchins are assembled by a large number of nanorod with 1–2 μm in length (Fig. 2b and 2e). Interestingly, when the $\text{g-C}_3\text{N}_4$ nanosheets were added into the reaction solution during the hydrothermal treatment process, the “nanograss” structure was established between $\text{W}_{18}\text{O}_{49}$ and $\text{g-C}_3\text{N}_4$. In this unique “nanograss” structure, the $\text{g-C}_3\text{N}_4$ nanosheets can be regarded as the “ground”, and the $\text{W}_{18}\text{O}_{49}$ are self-assembly on $\text{g-C}_3\text{N}_4$ nanosheets surface to present the “grasses”-like nanostructures. (Fig. 2c and 2f). Besides, it is interesting to see that the addition amount of $\text{g-C}_3\text{N}_4$ would affect the morphology of the composite. As shown in Fig. S1a, when the addition amount of $\text{g-C}_3\text{N}_4$ is insufficient, more $\text{W}_{18}\text{O}_{49}$ would gather together to form bigger nanograss on the surface of $\text{g-C}_3\text{N}_4$ nanosheets than that of WCN-3, but excessive $\text{g-C}_3\text{N}_4$ would lead to the formation of $\text{W}_{18}\text{O}_{49}$ nanograss with small size (Fig. S1b). The high-resolution TEM (HR-TEM) of the prepared $\text{W}_{18}\text{O}_{49}/\text{g-C}_3\text{N}_4$ composites in Fig. 2g shows that the $\text{g-C}_3\text{N}_4$ nanosheets present the amorphous structure, and the tungsten oxide ($\text{W}_{18}\text{O}_{49}$) nanograss on the $\text{g-C}_3\text{N}_4$ nanosheets owns the crystal lattices with the interplanar distance of 0.38 nm, which is in accordance with the lattice spacing of the (010) crystal plane of the monoclinic $\text{W}_{18}\text{O}_{49}$. The Fast Fourier transform (FFT) pattern further demonstrates the great crystal structure of the prepared $\text{W}_{18}\text{O}_{49}$ (Inset picture of Fig. 2g). EDS analysis shown in Fig. 2h means that the prepared sample consist C, N, O and W elements, and EDS mapping further confirmed the existence and the distribution of these elements mentioned (Fig. 3) These results are powerful evidences for the successful synthesis of $\text{W}_{18}\text{O}_{49}/\text{g-C}_3\text{N}_4$ composites.

3.2. Surface chemical composition and group analysis

The surface chemical composition of the prepared samples was investigated by the FTIR analysis. In Fig. 4a, pure $\text{W}_{18}\text{O}_{49}$ presents clear peaks locate at $600\text{--}780 \text{ cm}^{-1}$, belonging to the typical stretching vibration bands from O–W–O. Another typical peak appears on 950 cm^{-1} , which can be assigned to W=O. The peak appears on 1618 cm^{-1} could refer to the –OH of the absorbed water molecules [41,43,44]. As for $\text{g-C}_3\text{N}_4$ nanosheets, a set of obvious vibration peaks can be found, which belong to the CN heterocycles ($1200\text{--}1620 \text{ cm}^{-1}$) and s-triazine ring units (808 cm^{-1}) [27,42,45]. The prepared $\text{W}_{18}\text{O}_{49}/\text{g-C}_3\text{N}_4$ composites own the typical characteristic peaks of both $\text{g-C}_3\text{N}_4$ and $\text{W}_{18}\text{O}_{49}$ (Figs. 4a and S2). And meanwhile, when we make an in-depth analysis and comparison with the above feature curves originated from the $\text{g-C}_3\text{N}_4$ and $\text{W}_{18}\text{O}_{49}$ in the prepared WCN-3 (Fig. 4b), the vibration peak position of the s-triazine rings experiences a slight variation from 808 cm^{-1} to 811 cm^{-1} in WCN-3 sample, which indicates the possible structural distortion of “nitrogen pots” due to the chemical interaction occurred on the interface between $\text{g-C}_3\text{N}_4$ and $\text{W}_{18}\text{O}_{49}$.

X-ray photoelectron spectroscopy (XPS) spectrum of the prepared samples has also been provided to further investigate the interaction between $\text{g-C}_3\text{N}_4$ and $\text{W}_{18}\text{O}_{49}$. The survey XPS spectrum in Fig. 5a means that the prepared WCN-3 mainly composed of C, N, O and W elements.

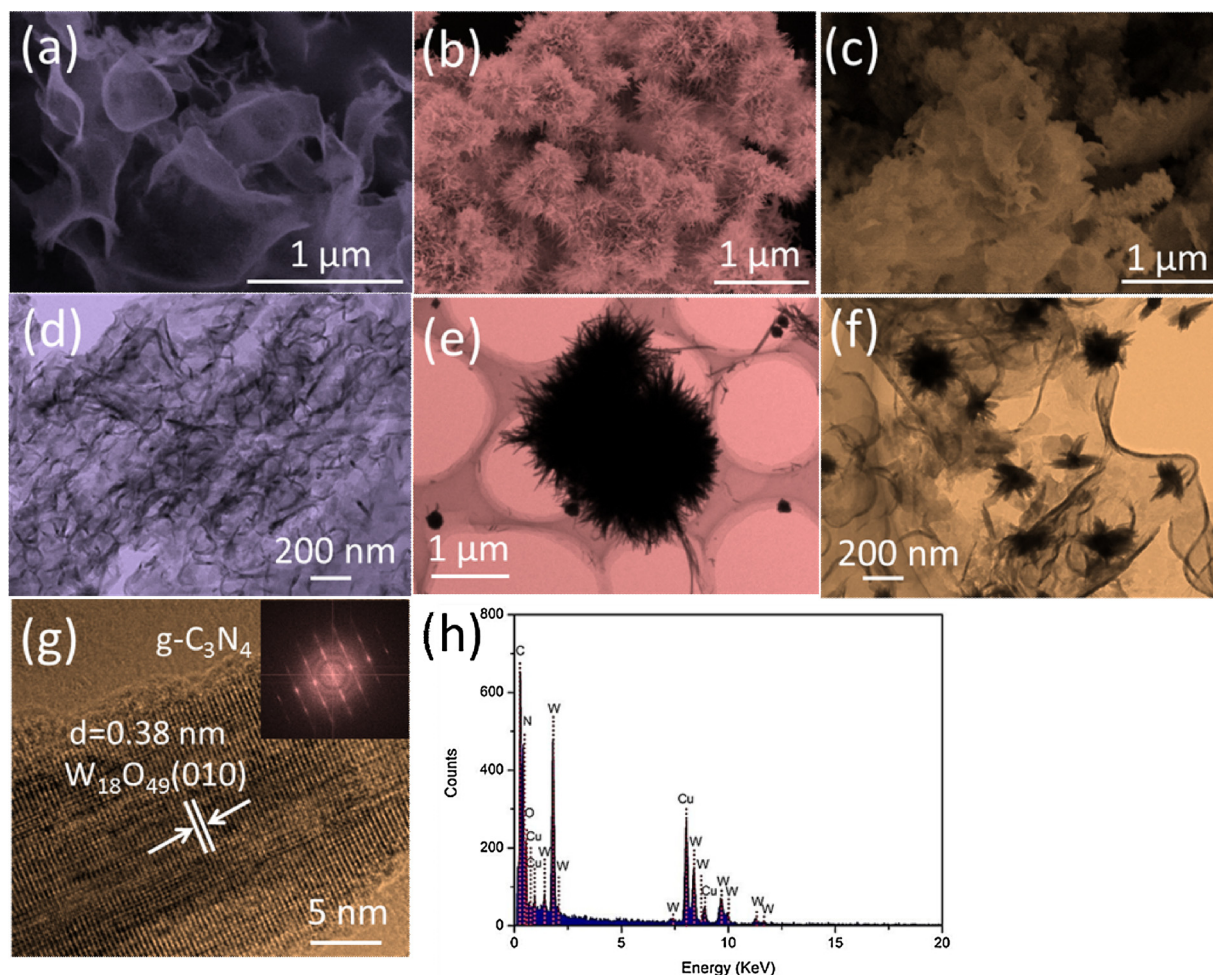


Fig. 2. SEM images of (a) g-C₃N₄ nanosheets, (b) W₁₈O₄₉ sea urchins composites and (c) WCN-3; TEM images of (d) g-C₃N₄ nanosheets, (e) W₁₈O₄₉ sea urchins composites and (f) WCN-3; (g) HR-TEM image of WCN-3 (corresponding Fast Fourier transform images present in the inset picture); and (h) EDS analysis of the prepared WCN-3.

Fig. 5b–e shows the high-resolution spectra of W 4f, O 1s, C 1s and N 1s. As for pure W₁₈O₄₉, we can see that the spectra of W 4f can be divided into four peaks. The two peaks with the binding energy of 37.69 eV and 35.69 eV are contributed to 4f_{5/2} and 4f_{7/2} of W⁶⁺, and the other two peaks locate at 36.64 eV and 34.34 eV are attributed to 4f_{5/2} and 4f_{7/2} of W⁵⁺ [32]. The high-resolution spectra of O 1s for pure W₁₈O₄₉ can be assigned to two peaks, which are belong to W–O (530.34 eV) and –OH (531.75 eV) stemming from the absorbed water molecules. But for the prepared WCN-3, a new peak with the binding energy of 532.84 eV appears on the spectra, which attributes to the interaction between g-C₃N₄ and W₁₈O₄₉ during the preparation process. As for pure g-C₃N₄ nanosheets, in Fig. 5d, the main peak in the C 1s spectra locates at 288.04 eV belongs to sp²-hybridized carbon in an N-containing aromatic ring (N–C=N), and another weak peak with the binding energy of 284.65 eV can be identified to the sp² C–C bond [42]. The N 1s of g-C₃N₄ can be divided into four peaks, which correspond to the sp²-hybridized nitrogen in C-containing triazine rings (C–N=C) (398.59 eV), the tertiary nitrogen (N–(C)3) (400.39 eV), amino groups (C–N–H) (401.24 eV) and charging effects of positive charge location (404.29 eV) [42]. As for the prepared WCN-3 sample, it contains all the feature peaks appeared on the spectra of pure W₁₈O₄₉ or g-C₃N₄ nanosheets, which demonstrate the successful preparation of W₁₈O₄₉/g-C₃N₄ nanocomposites once again. But the difference is that characteristic peaks of both g-C₃N₄ and W₁₈O₄₉ experience a shift process after form the W₁₈O₄₉/g-C₃N₄ nanograss structure. As shown in Fig. 5b and 5c, we can see that the peak signals of W 4f and O 1s in WCN-3 shift to higher

banding energy than the corresponding values of the pure W₁₈O₄₉ sample. On the contrary, the relative peak signals of C 1s and N 1s shift to lower binding energy than that of pure g-C₃N₄. It should be noted that the increase of binding energy indicates the weakened electron screening effect due to the decrease of the electron concentration, whereas the decrease of binding energy means the increase of electron concentration [46,47]. So the changes of the binding energy of the characteristic peaks indicated the electron transfer process would happen on the W₁₈O₄₉/g-C₃N₄ heterointerface, and the photogenerated electrons tends to move from W₁₈O₄₉ to g-C₃N₄, which can be served as an strong evidence for the propose of the Z-scheme reaction mechanism.

3.3. Optical properties

To investigate the light harvesting ability of the prepared samples, the UV–vis–NIR absorption spectra are provided and shown in Fig. 6a. It can be seen that the light absorption edge of pure g-C₃N₄ nanosheets is located at around 460 nm, and the prepared W₁₈O₄₉ sea urchin presents the absorption edge of 440 nm. Besides, the prepared W₁₈O₄₉ presents a very broad absorption tail starting from 450 to 1500 nm, indicating the strong absorption ability in the range of visible light and NIR light. The unique absorption tail of W₁₈O₄₉ sample is stem from the metal-like LSPR induced by the collective oscillations of excess charges (electrons) on the surface of tungsten oxide due to the abundant oxygen vacancies [35,37]. Then after the adhere of W₁₈O₄₉ on the surface of g-C₃N₄

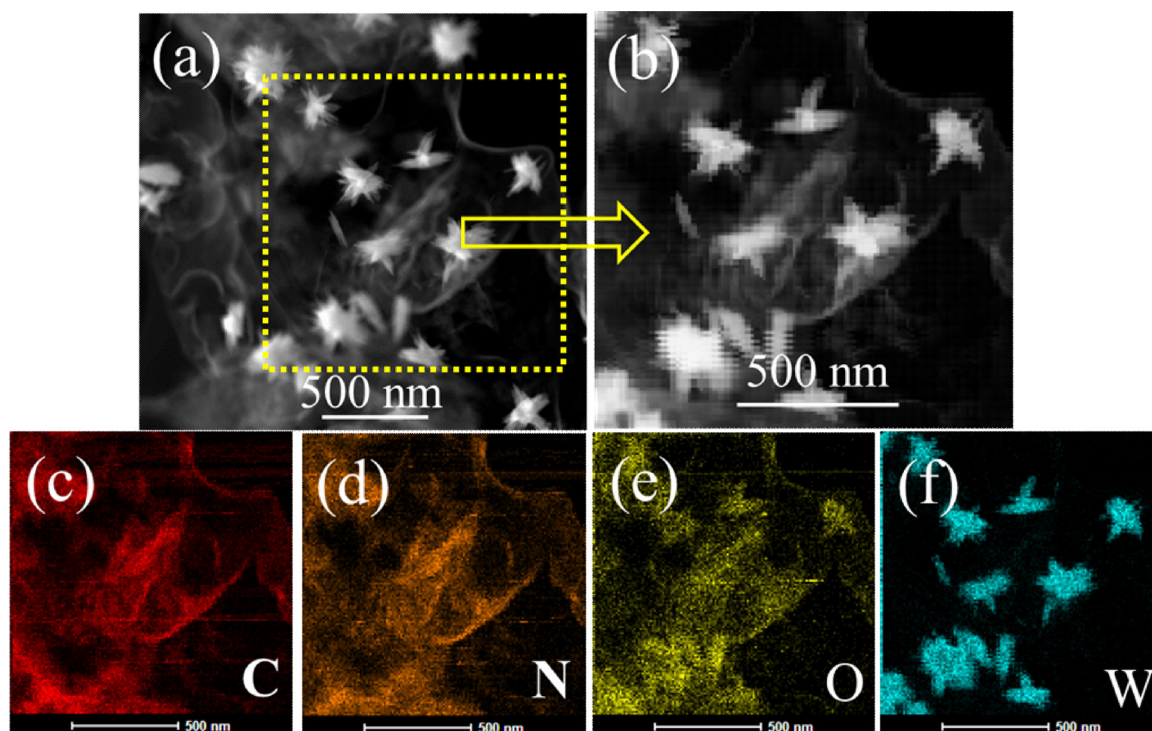


Fig. 3. (a, b) HAADF-STEM image of WCN-3, and (c–f) corresponding EDS mapping of C, N, O and W.

nanosheets for the formation of $W_{18}O_{49}/g-C_3N_4$ nanograin, the absorption tail in the range of visible to NIR light can also be found, indicating the full-solar-spectrum light response ability of the $W_{18}O_{49}/g-C_3N_4$ nanograin composites. Besides, it can be seen that more $g-C_3N_4$ content in the prepared $W_{18}O_{49}/g-C_3N_4$ would lead to the decrease of its light response ability in the vis-NIR light regions.

In order to fully understand the change of the light absorption ability, the band gap (E_g) of $W_{18}O_{49}$ and $g-C_3N_4$ has been calculated via the following formula [42]:

$$ah\nu = A(h\nu - E_g)^{n/2} \quad (1)$$

where a , h , ν , E_g and A are absorption coefficient, planck constant light frequency, band gap energy, and a constant, respectively. According to the results shown in Fig. 6b and 6c, the E_g of $g-C_3N_4$ and $W_{18}O_{49}$ are estimated to be 2.78 eV and 2.89 eV, respectively. Moreover, to further investigate the valence band of the prepared $g-C_3N_4$ and $W_{18}O_{49}$, the XPS valence band data were collected and presented in Fig. 6d and 6e,

from which we can see that the valence band (E_{VB}) of $g-C_3N_4$ and $W_{18}O_{49}$ are calculated to be 1.59 eV and 3.24 eV, respectively. So according to the results mentioned above, the conduction band (E_{CB}) of the prepared samples can be estimated based on the following equation [45]:

$$E_{CB} = E_{VB} - E_g \quad (2)$$

Therefore, the E_{CB} of $g-C_3N_4$ and $W_{18}O_{49}$ are -1.19 eV and 0.35 eV, respectively. These data are useful for the analysis of the reaction process between $g-C_3N_4$ and $W_{18}O_{49}$, and have been fully discussed in the reaction mechanism discussion part.

3.4. Photogenerated charge transportation and separation properties

The steady-state photoluminescence (PL) emission spectra of the prepared $g-C_3N_4$ and WCN-3 sample are shown in Fig. 7a. The higher PL intensity means the higher recombination rate of the photogenerated

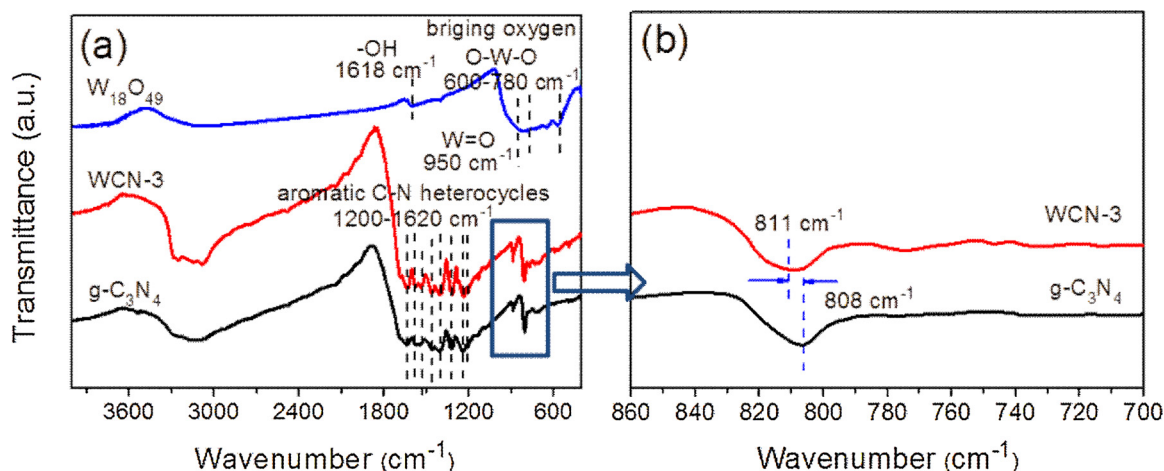


Fig. 4. FTIR of the prepared $g-C_3N_4$, $W_{18}O_{49}$ and WCN-3.

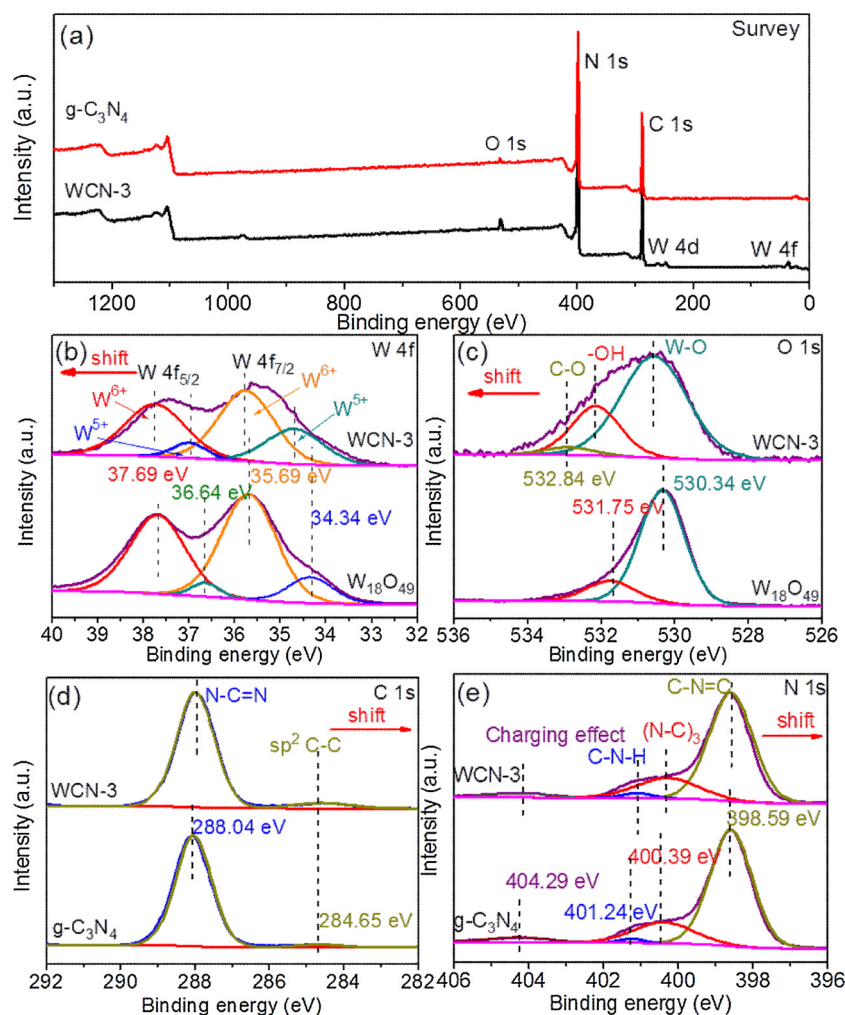


Fig. 5. The XPS spectra of the prepared g-C₃N₄, W₁₈O₄₉ and WCN-3. (a) survey, (b) W 4f, (c) O 1s, (d) C 1s and (e) N 1s.

charges. In Fig. 7a, we can see that the prepared g-C₃N₄ shows high PL peak intensity, which means the high recombination rate of the photogenerated electrons and holes. But for the prepared WCN-3 sample, the relative peak intensity decrease dramatically, indicating that the recombination rate of photogenerated charges have been inhibited greatly after the assembly of W₁₈O₄₉ on the surface of g-C₃N₄ nanosheets. It should be noted that the prepared W₁₈O₄₉ showed the lowest PL peaks, which does not mean that W₁₈O₄₉ owns excellent charge separation rate, because the PL responses of different semiconductors are different which cannot be compared simply according to charge separation rate. And this phenomenon also can be observed in many other researchers' study [48–51]. In our study, it's obvious that after the combination with W₁₈O₄₉, the PL intensity of g-C₃N₄ decreased significantly, which can be a strong evidence for the increased charge separation rate of g-C₃N₄. The transient photocurrent (I-t) and electrochemical impedance spectroscopy (EIS) measurement have also been conducted for the comprehensive study of the photo-response ability and photogenerated charges recombination efficiency of the photocatalyst. As shown in Fig. 7b, under the irradiation of the light irradiation, all the samples present rapid and stable photocurrent response. But the prepared WCN-3 presents higher photocurrent density than that of pure g-C₃N₄ and W₁₈O₄₉, indicating the higher light harvesting and low photogenerated charges recombination efficiency. EIS is an efficient electrochemical method to explain the electron-transfer efficiency of the photocatalysts. Fig. 7c shows the results that g-C₃N₄ present the biggest diameter, implying higher recombination efficiency and poor electrical conductivity, which inhibiting the electron transfer

of the sample. In comparison, the prepared WCN-3 presents the smallest diameter, implying the lowest charge transfer impedance and recombination efficiency of the photogenerated charges.

To mine more information about the photogenerated charges, the time-resolved transient PL (TRPL) decay curves of the prepared g-C₃N₄ and WCN-3 sample have been measured. As shown in Fig. 7d, the data can be transferred and described according to the following function [52]:

$$I(t) = A_1 \exp(-t/\tau_1) + A_2 \exp(-t/\tau_2) \quad (3)$$

where A_1 and A_2 are the weight factor, and τ_1 and τ_2 are the corresponding fluorescent lifetime. In Table 1, the fast lifetime component (τ_1) are stemmed from the non-radiative recombination of photogenerated electrons near the surface with defects, and the low lifetime component (τ_2) are assigned to the radiative recombination of excitons from the defect-free regions within the g-C₃N₄ nanosheets. It is clearly to see that τ_1 and τ_2 for WCN-3 sample is 2.22 ns and 7.45 ns, respectively, and they are longer than that of pure g-C₃N₄ nanosheets ($\tau_1 = 1.86$ ns; $\tau_2 = 5.42$ ns). Herein, we can obtain the average fluorescent lifetime of g-C₃N₄ and WCN-3 via the following equation [52]:

$$\tau_A = \frac{A_1 \tau_1^2 + A_2 \tau_2^2}{A_1 \tau_1 + A_2 \tau_2} \quad (4)$$

The results in Table 1 shown that the average fluorescent lifetime of WCN-3 (6.39 ns) is longer than that of g-C₃N₄ nanosheets (4.86 ns), indicating that after adhering the W₁₈O₄₉ on the surface of g-C₃N₄, the

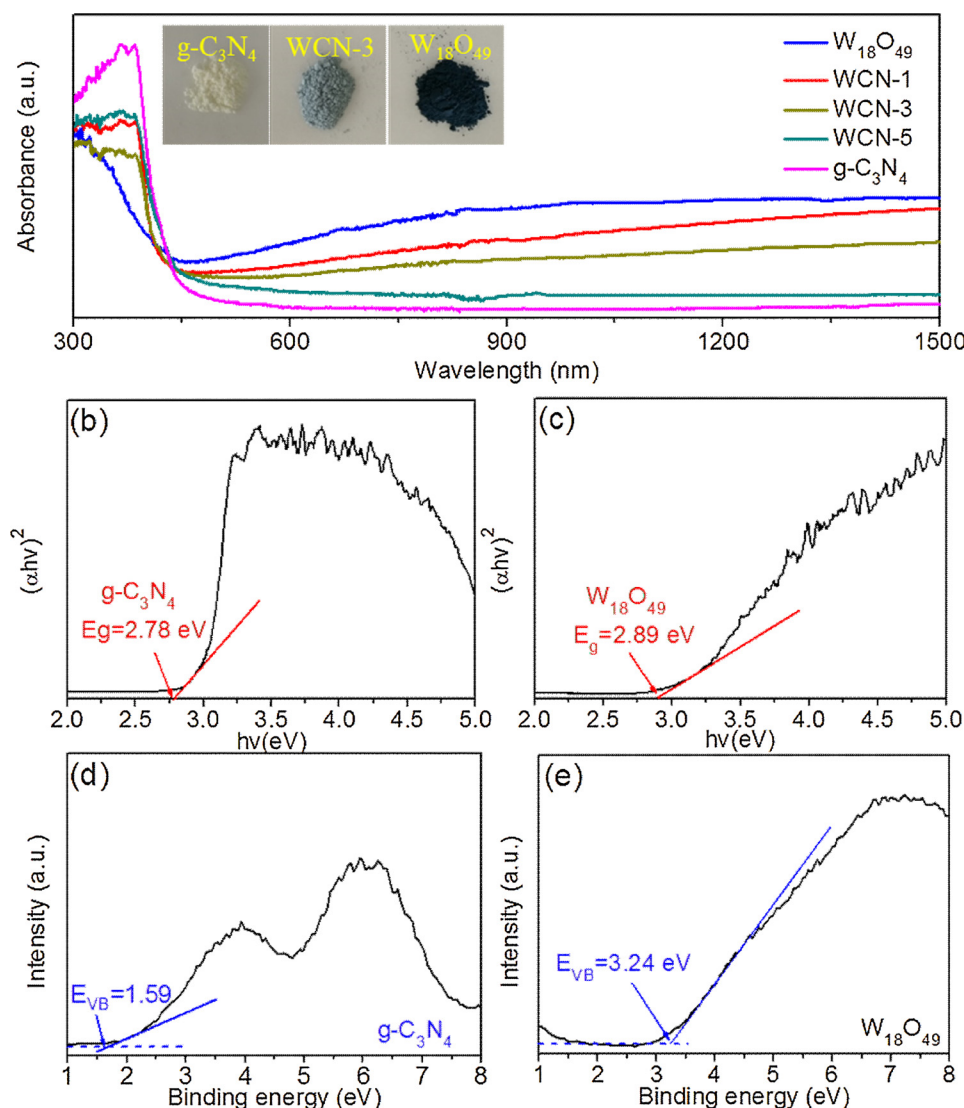


Fig. 6. (a) UV-vis-NIR diffuse reflectance spectra of the prepared $W_{18}O_{49}$, WCN-3 and $g-C_3N_4$ (inset picture are the photographs of the prepared samples); (b and c) the band gap energy and (d and e) VB XPS spectra of $g-C_3N_4$ and $W_{18}O_{49}$.

fluorescent lifetime can be prolonged. The prolonged charge carrier lifetime means the fast transportation and the inhibited recombination efficiency of the photogenerated charges, which is important for the enhanced photocatalytic activity.

3.5. Photocatalytic activity of the prepared photocatalysts

The photocatalytic performance of the prepared $W_{18}O_{49}/g-C_3N_4$ nanograin composites was investigated by the degradation of colorful MB and colorless CIP. Before photocatalytic degradation process, the adsorption experiments under dark condition were carried out to study the adsorption ability of different photocatalysts. Results showed that the adsorption-desorption equilibrium between photocatalysts and contaminant molecules can be achieved within 30 min. Fig. 8a shows the results of MB degradation based on the as-prepared $W_{18}O_{49}/g-C_3N_4$ composites. It can be seen that just 69.3% of MB is degraded with the existence of pure $W_{18}O_{49}$, and for pure $g-C_3N_4$, only 86.8% of MB can be removed after 60 min full-spectrum irradiation ($\lambda > 365$ nm). When the prepared $W_{18}O_{49}/g-C_3N_4$ nanograin composites were added into the reaction system, the photocatalytic removal efficiency is boosted. In Fig. 8a, it can be observed that the prepared WCN-3 presents the highest photocatalytic activity, degrading nearly all the MB

molecules within 40 min. Excessive or insufficient addition of $g-C_3N_4$ in prepared process would lead to the reduction of the eventual photocatalytic activity. This phenomenon can be explained by two reasons as follows. On one hand, when the addition of $g-C_3N_4$ is insufficient, more $W_{18}O_{49}$ would be gathering together to form big nanograin, resulting in the limited contact between $g-C_3N_4$ nanosheet and $W_{18}O_{49}$, so the synergistic effect cannot reach the optimum condition and the transportation process of photogenerated electrons and holes also would be strictly inhibited. On the other hand, when the addition amount of $g-C_3N_4$ is excessive, the relative content of $W_{18}O_{49}$ in the $W_{18}O_{49}/g-C_3N_4$ composite would decrease, which may result in the reduction of plasma resonance effect in the reaction process. Additionally, more $g-C_3N_4$ would hinder the light absorption effect of $W_{18}O_{49}$, leading to low photocatalytic activity.

Besides, the photocatalytic degradation kinetics of MB under full-spectrum light irradiation was investigated, and the results showed that the changes of MB concentration versus the reaction time over $W_{18}O_{49}/g-C_3N_4$ hybrid materials followed pseudo-first-order kinetics plot by the equation of $-\ln(C/C_0) = kt$, where t , C_0 , and C are the reaction time, initial MB concentration (mg/L), MB concentration at time t (mg/L); k represents the apparent pseudo-first-order rate constant (min^{-1}). In Fig. 8b, it can be seen that WCN-3 owns the maximum rate constant of

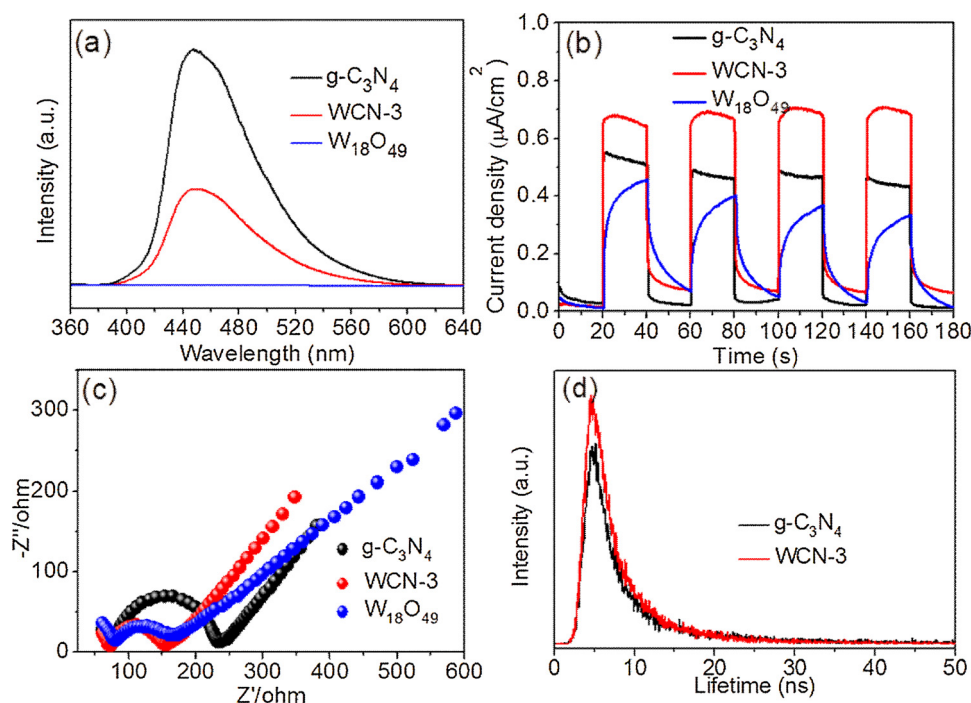


Fig. 7. (a) Photoluminescence spectra (b) photocurrent response (c) EIS Nyquist plots and (d) time-resolved transient photoluminescence (TRPL) spectra of the prepared samples.

Table 1

Dynamics analysis of emission decay for the different samples.

Samples	A ₁ (%)	τ ₁ (ns)	A ₂ (%)	τ ₂ (ns)	τ _A (ns)
g-C ₃ N ₄	34.92	1.86	65.08	5.42	4.86
WCN-3	45.84	2.22	54.16	7.45	6.39

0.0677 min⁻¹, which is about 3 times and 5 times higher than that of g-C₃N₄ (0.0276 min⁻¹) and W₁₈O₄₉ (0.0148 min⁻¹), respectively. TOC removal experiments have also been conducted to study the mineralization ability of this reaction system. As shown in Fig. S3, under full-spectrum light irradiation for 60 min, 26.86% of TOC can be removed in the presence of g-C₃N₄, and for W₁₈O₄₉, only 11.28% TOC removal efficiency can be achieved. It should be noted that under the similar condition, the TOC removal efficiency based on WCN-3 sample can reach 40.18%, which is higher than those of g-C₃N₄ and W₁₈O₄₉. The

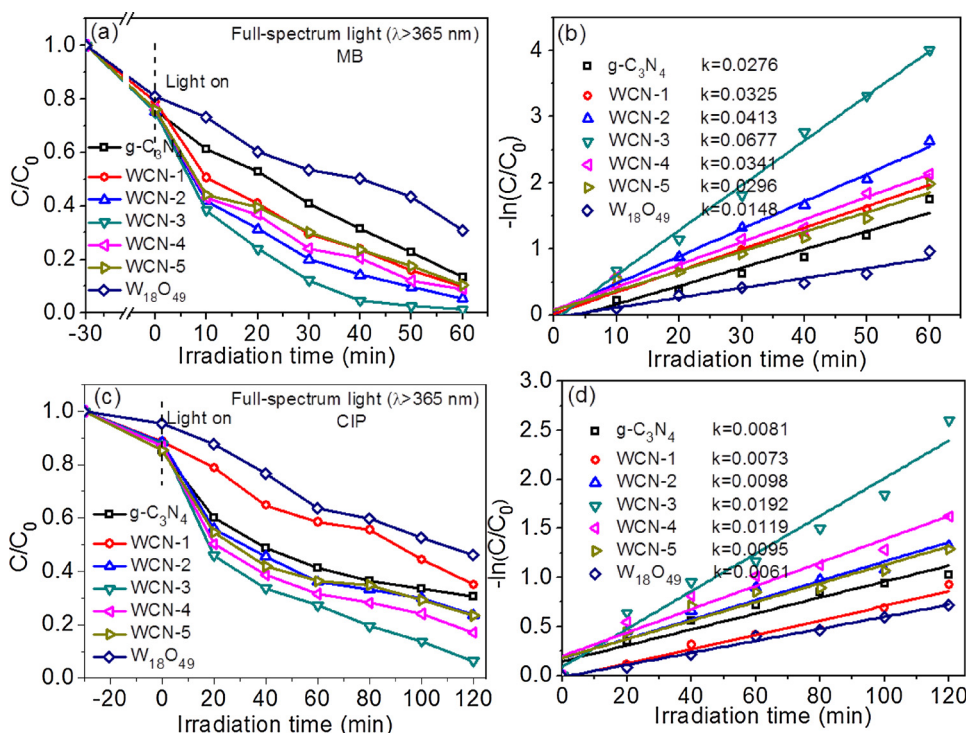


Fig. 8. (a) Photocatalytic degradation of MB with different photocatalysts under full-spectra light irradiation ($\lambda > 365$ nm) and (b) the corresponding pseudo-first-order kinetic plots; (c) Photodegradation of CIP with different photocatalysts under full-spectra light irradiation ($\lambda > 365$ nm) and (d) the corresponding pseudo-first-order kinetic plots.

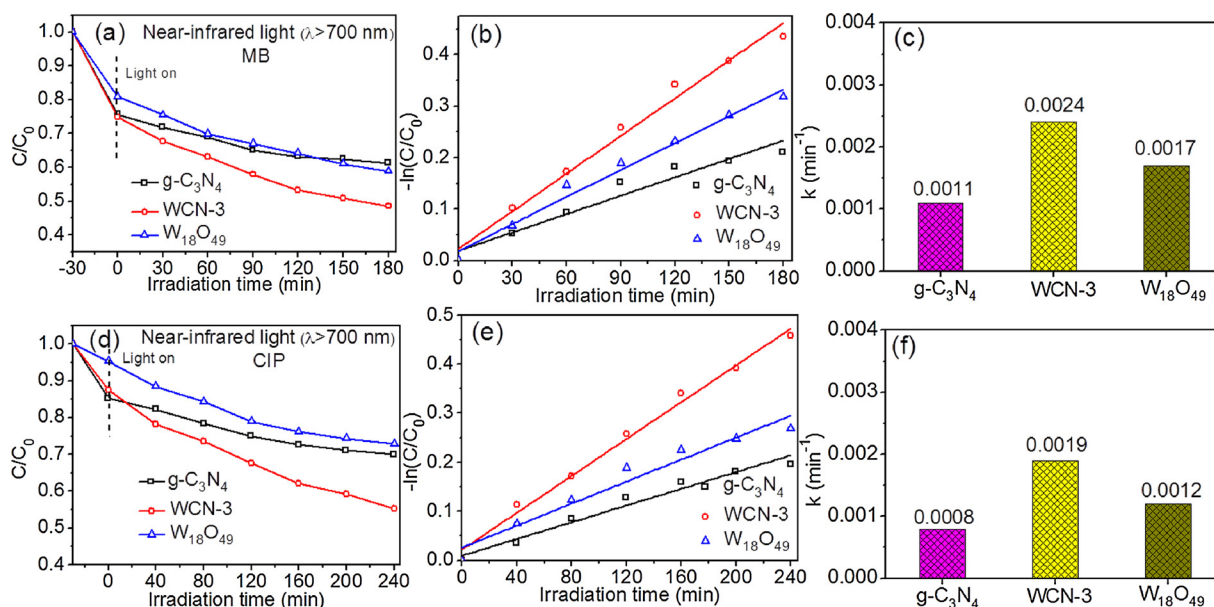


Fig. 9. (a) Photocatalytic degradation of MB based on the prepared $g-C_3N_4$, WCN-3 and $W_{18}O_{49}$ under NIR light ($\lambda > 700$ nm) and (b) the relative pseudo-first-order kinetic plots and (c) kinetic constants; (d) photocatalytic degradation CIP of MB based on the prepared $g-C_3N_4$, WCN-3 and $W_{18}O_{49}$ under NIR light ($\lambda > 700$ nm) and (e) the relative pseudo-first-order kinetic plots and (f) kinetic constants.

experiment results demonstrate that the prepared $W_{18}O_{49}/g-C_3N_4$ composites can not only photodegrade the MB molecules, but also decompose the MB molecules into CO_2 and H_2O .

To shield the effect of dye sensitization in the photocatalytic process, CIP, an antibiotic and colorless contaminants in our environment, have also been chosen as the target pollutant. As shown in Fig. 8c, with the existence of $W_{18}O_{49}$, only 53.8% of CIP can be degraded under full-spectrum light ($\lambda > 365$ nm) irradiation for 120 min. As for $g-C_3N_4$, 69.2% of CIP can be removed under the same condition. When the prepared $W_{18}O_{49}/g-C_3N_4$ nanograin composites were added, the CIP removal efficiency increased. Similarly, the WCN-3 shows the highest photodegradation efficiency towards CIP and the removal efficiency can reach to 93.5% after 120 min full-spectrum light irradiation. The reaction kinetics of CIP also followed pseudo-first-order kinetics plot. Fig. 8d discloses that the rate constant for WCN-3 is 2 and 3 times higher than that of $g-C_3N_4$ and $W_{18}O_{49}$, which implies that the prepared $W_{18}O_{49}/g-C_3N_4$ nanograin composites own great potential for future realistic wastewater treatment.

Additionally, the photocatalytic activity of the prepared $g-C_3N_4$, WCN-3 and $W_{18}O_{49}$ have been further investigated under NIR light irradiation. As shown in Fig. 9a, under NIR light irradiation ($\lambda > 700$ nm), the photocatalytic activity of the prepared pristine $g-C_3N_4$ was greatly inhibited due to the low photon energy. But different

from the results shown in Fig. 8, the prepared $W_{18}O_{49}$ presents enhanced photocatalytic activity than that of pristine $g-C_3N_4$ due to the LSPR effect. Besides, we found that the photocatalytic activity of the prepared WCN-3 still presents higher photocatalytic performance than that of pristine $g-C_3N_4$ and $W_{18}O_{49}$, presenting 51.5% of MB degradation efficiency under NIR light irradiation for 180 min. The rate constant result disclosed in Fig. 9b and 9c shows that WCN-3 presents the highest rate constant (0.0024 min^{-1}), which is about 2 times and 1.5 times higher than that of $g-C_3N_4$ and $W_{18}O_{49}$, respectively. Fig. 9d shows that photocatalytic degradation efficiency of WCN-3 towards CIP degradation is also higher than that of $g-C_3N_4$ and $W_{18}O_{49}$, achieving 44.7% removal efficiency of CIP under NIR light irradiation for 240 min. Meanwhile, WCN-3 owns a rate constant of 0.0019 min^{-1} , which is 2 times higher than that of $g-C_3N_4$ (0.0008 min^{-1}) and nearly 1.5 times higher than that of $W_{18}O_{49}$ (0.0012 min^{-1}). The results mentioned above indicated that the prepared $W_{18}O_{49}/g-C_3N_4$ nanograin presents great photocatalytic activity in both full-spectrum light and NIR light irradiation.

As for realistic application, the reusability and stability of the photocatalysts is very important, so the recycling reaction experiments based on WCN-3 for the degradation CIP have been conducted to evaluate the stability of the prepared $W_{18}O_{49}/g-C_3N_4$ nanograin composite. As shown in Fig. 10, after five recycle experiments, the

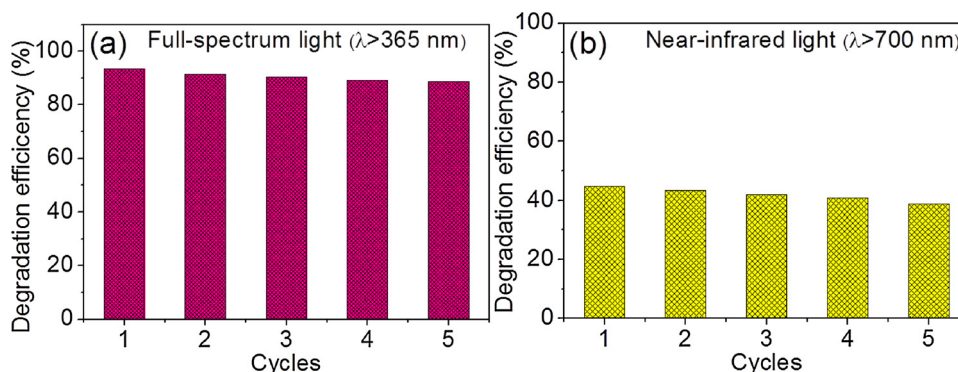


Fig. 10. Recycle experiments of WCN-3 composite for the degradation of CIP (a) under full-spectrum light irradiation ($\lambda > 365$ nm) for 120 min and (b) under near-infrared light irradiation ($\lambda > 700$ nm) for 480 min.

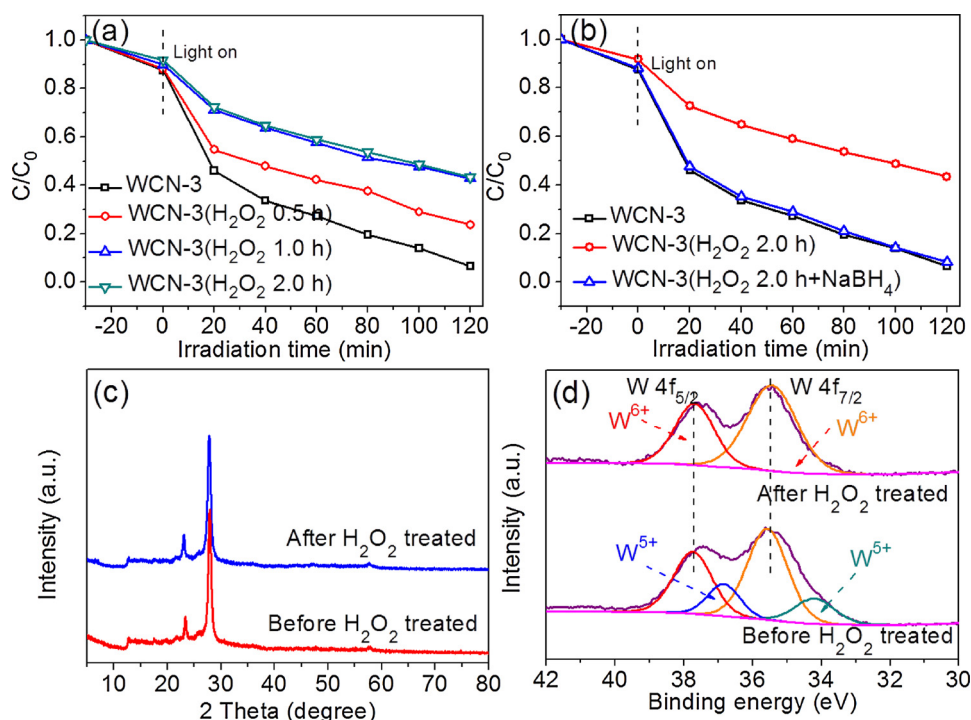


Fig. 11. (a) Photocatalytic degradation process of CIP with WCN-3 or the samples treated with H_2O_2 for different time under full-spectrum light irradiation; (b) photocatalytic degradation process of CIP with WCN-3, WCN-3 oxidized with H_2O_2 for 2 h and WCN-3 oxidized with H_2O_2 for 2 h and further treated with $NaBH_4$ aqueous solution. (c) XRD patterns of the WCN-3 sample before and after H_2O_2 oxidation process and (d) XPS spectra of the WCN-3 sample before and after H_2O_2 oxidation process.

photocatalytic activity of WCN-3 did not experience an obvious decrease process under both full-spectrum light and NIR light irradiation, indicating the high stability of the prepared $W_{18}O_{49}/g-C_3N_4$ nanograin composite.

3.6. The evaluation of the role of oxygen vacancies

It is well known that the oxygen vacancies play vital role for the enhanced photocatalytic activity of the $W_{18}O_{49}$ based materials. Hence, we investigated the photocatalytic activity of the oxygen-vacancy-rich WCN-3 nanocomposite by the photocatalytic degradation of CIP under full-spectrum light irradiation [40,41]. In this study we rational designed control experiments to investigate the function of oxygen vacancies. First of all, we used the hydrogen peroxide (H_2O_2) to oxide the prepared WCN-3 to eliminate the oxygen vacancies on its surface. As shown in Fig. 11a, when WCN-3 was treated with H_2O_2 for 0.5 h, the photocatalytic activity was inhibited, and when the treatment time was extended to 1.0 h, the photocatalytic activity further decreased. But keep prolonging the H_2O_2 treatment time to 2.0 h, the photocatalytic activity of WCN-3 did not decrease anymore, indicating that the surface of WCN-3 was thoroughly oxide with 1.0 h hydrogen peroxide treatment and oxygen vacancies nearly disappear on WCN-3 surface. Interestingly, although the photocatalytic activity of WCN-3 has been inhibited greatly owing to the oxidation treatment process of H_2O_2 , the corresponding activity can be nearly recovered via the $NaBH_4$ reduction treatment process. As shown in Fig. 11b, after the treatment of oxidized WCN-3 sample with 0.1 M $NaBH_4$ aqueous solution for 2.0 h, the relative photocatalytic activity can be recovery and even equal to the pristine WCN-3 sample, implying that the reduction treatment of $NaBH_4$ can re-generate the oxygen vacancies on the surface of WCN-3. Then to make in-depth investigation for reasons of the decrease photocatalytic activity of the H_2O_2 treated WCN-3, XRD and XPS of the WCN-3 before and after H_2O_2 oxidation have been investigated. As shown in Fig. 11c, the XRD pattern of WCN-3 before and after H_2O_2 treatment did not show obvious change, indicating that the crystal structure of the WCN-3 was not change after the treatment of H_2O_2 . After the analysis of the valance of W atoms in WCN-3 before and after H_2O_2 treatment via XPS spectroscopy, we found that great changes have

happened. In Fig. 11d, it can be seen that for pristine WCN-3, four peaks refer to W4f could be found in the XPS spectrum, assigning to W^{6+} and W^{5+} of W atoms. The unsaturated valance state of W atoms means the existence of oxygen vacancies on the surface of WCN-3. For the H_2O_2 treated WCN-3, only two sharp peaks of W4f can be observed, which belongs to the typical characteristic peaks of W^{6+} . This phenomenon means the disappearance of oxygen vacancies in the surface of WCN-3 after oxidized by H_2O_2 . It should be noted that changes only happened on W atoms state of the oxidized WCN-3 but not on the XRD pattern, which clearly illustrated that only the surface of the sample was oxidized, and the inside of the WCN-3 sample was still composite of $g-C_3N_4$ and $W_{18}O_{49}$. The results discussed above indicated that the oxygen vacancies dramatically influence the photocatalytic activity of $W_{18}O_{49}/g-C_3N_4$ nanograin composite.

3.7. Photocatalytic reaction mechanism

To study the electron transfer and reaction mechanism, trapping radical control experiments have been conducted for the degradation of CIP based on WCN-3 composite. As shown in Fig. 12a, it can be seen that when 1,4-benzoquinone (BQ) was added in the reaction system, the photocatalytic degradation efficiency of CIP under full-spectrum light irradiation ($\lambda > 365$ nm) was inhibited greatly, indicating that $\cdot O_2^-$ radical species play vital role in the photocatalytic degradation process. Similarly, when the isopropanol (IPA) or triethanolamine (TEOA) were added, the photocatalytic activity of WCN-3 also decreased greatly, implying that $\cdot OH$ and h^+ also influence the removal efficiency of CIP greatly. Then ESR spin-trap measurement based on WCN-3 was also conducted to further definitely affirm the generation of $\cdot O_2^-$ and $\cdot OH$ species. In Fig. 12b, under the irradiation of full-spectrum light, some characteristic peaks of DMPO- $\cdot O_2^-$ can be observed, indicating that $\cdot O_2^-$ radical species were generated in WCN-3 based reaction system. However, no signals appear under dark condition. Similarly, four characteristic peaks of DMPO- $\cdot OH$ adducts also can be founded under full-spectrum light irradiation in the presence of WCN-3. (Fig. 12c) The radical trapping experiment and ESR results demonstrated that h^+ , $\cdot O_2^-$ and $\cdot OH$ radical species all generated in the reaction system and participated in the CIP degradation based on WCN-3 under full-

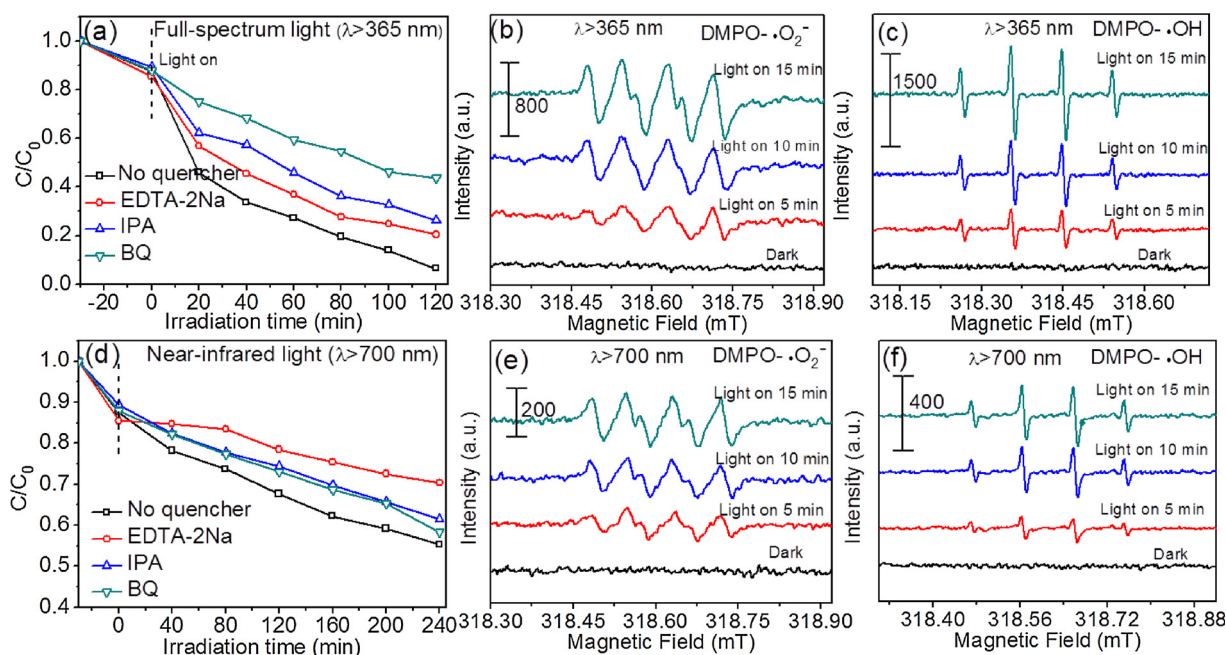


Fig. 12. (a) Trapping experiments for the photocatalytic degradation of CIP and (b and c) ESR spectra of radical adducts trapped by DMPO ($\cdot\text{O}_2^-$ and $\cdot\text{OH}$) under full-spectra light irradiation ($\lambda > 365$ nm); (d) trapping experiments for the photocatalytic degradation of CIP and (e and f) ESR spectra of radical adducts trapped by DMPO ($\cdot\text{O}_2^-$ and $\cdot\text{OH}$) under near-infrared light irradiation ($\lambda > 700$ nm).

spectrum light irradiation.

Moreover, to make comprehensive understanding of the reaction mechanism of the prepared $\text{W}_{18}\text{O}_{49}/\text{g-C}_3\text{N}_4$ nanograss composites under different irradiation condition, the trapping experiments and ESR measurement also have been conducted under NIR light irradiation ($\lambda > 700$ nm). As shown in Fig. 12d, the photocatalytic degradation of CIP based on WCN-3 have been greatly inhibited in the presence of TEOA, indicating that h^+ plays the major role for CIP degradation under NIR light irradiation. It should be noted that the addition of BQ and IPA also bring about negative effect of CIP degradation, indicating that the $\cdot\text{O}_2^-$ and $\cdot\text{OH}$ radical species also participate in the degradation process under NIR light irradiation. The ESR results shown in Fig. 12e and 12f confirm the generation of $\cdot\text{O}_2^-$ and $\cdot\text{OH}$ radical species under NIR light irradiation based on WCN-3 composites as well, though the radical peak intensity of these radical species under NIR light is lower than that under full-spectrum light irradiation.

Therefore, based on these experimental results, the reaction mechanism of the prepared $\text{W}_{18}\text{O}_{49}/\text{g-C}_3\text{N}_4$ nanocomposite is proposed and illustrated in Fig. 13. As shown in Fig. 13a, under full-spectrum light irradiation, both $\text{g-C}_3\text{N}_4$ and $\text{W}_{18}\text{O}_{49}$ can be excited to generate photogenerated electrons and holes. The trapping radical experiment results and relative ESR analysis have demonstrated the generation of $\cdot\text{O}_2^-$ and $\cdot\text{OH}$ radical species, so the traditional band-to-band heterojunction is not appropriate to explain the reaction mechanism study. Because if the prepared $\text{W}_{18}\text{O}_{49}/\text{g-C}_3\text{N}_4$ nanograss composites follow the traditional heterojunction, the photogenerated electrons tends to transfer from E_{CB} of $\text{g-C}_3\text{N}_4$ to the E_{CB} of $\text{W}_{18}\text{O}_{49}$, and the photogenerated holes tends to migrate from E_{VB} of $\text{W}_{18}\text{O}_{49}$ to the E_{VB} of $\text{g-C}_3\text{N}_4$. However, the E_{CB} of $\text{W}_{18}\text{O}_{49}$ was not more negative than the $\text{O}_2/\cdot\text{O}_2^-$ potential (ca. -0.33 eV), and the E_{VB} of $\text{g-C}_3\text{N}_4$ was not more positive than that of $\text{OH}/\cdot\text{OH}$ potential ($+2.4$ eV) [27,45], so the $\cdot\text{O}_2^-$ and $\cdot\text{OH}$ radical species cannot generate at this condition. Combined with conclusions in the XPS analysis, the electron transfer process would happen between $\text{g-C}_3\text{N}_4$ and $\text{W}_{18}\text{O}_{49}$, and the electrons tend to transfer from $\text{W}_{18}\text{O}_{49}$ to $\text{g-C}_3\text{N}_4$, the Z-scheme reaction mechanism would be more suitable to explain the high photocatalytic activity of the prepared $\text{W}_{18}\text{O}_{49}/\text{g-C}_3\text{N}_4$ nanograss composites. That is to say, under full-spectrum light irradiation, both $\text{g-C}_3\text{N}_4$ and $\text{W}_{18}\text{O}_{49}$ would be

photoexcited, and the photogenerated electrons in the E_{CB} of $\text{W}_{18}\text{O}_{49}$ tend to recombine with the photogenerated holes generated on the E_{VB} of $\text{g-C}_3\text{N}_4$. Then the photogenerated electrons can retain on the E_{CB} of $\text{g-C}_3\text{N}_4$ and owns the strong reduction ability to react with O_2 for the formation of $\cdot\text{O}_2^-$. The photogenerated holes can keep at the E_{VB} of $\text{W}_{18}\text{O}_{49}$ and have the strong oxidation ability for the formation of $\cdot\text{OH}$ radical species. Besides, the former mentioned oxygen vacancies on the surface of $\text{W}_{18}\text{O}_{49}$ would bring about the LSPR effect under long wavelength light, generating hot electrons to inject into the E_{CB} of $\text{g-C}_3\text{N}_4$, which can increase the electron density and promote the eventually photocatalytic performance. So the dual-channel charge-carrier transfer path contributed to the boosted photocatalytic performance of the prepared $\text{W}_{18}\text{O}_{49}/\text{g-C}_3\text{N}_4$ nanograss composites. Additionally, the nanograss structure of the prepared $\text{W}_{18}\text{O}_{49}/\text{g-C}_3\text{N}_4$ composites would lead to more light reflection and refraction process, resulting in more light absorption and utilization, which also can bring about positive effect on the photocatalytic activity.

When the prepared $\text{W}_{18}\text{O}_{49}/\text{g-C}_3\text{N}_4$ nanograss composite was placed under NIR light irradiation ($\lambda > 700$ nm), the reaction mechanism is different. Under NIR light irradiation, only $\text{W}_{18}\text{O}_{49}$ can be excited and produce photogenerated electrons and holes. The trapping experiments have demonstrated the generation of both $\cdot\text{O}_2^-$ and $\cdot\text{OH}$ radical species, so the reaction mechanism can be interpreted in Fig. 13b. We can see that under NIR light irradiation, $\text{W}_{18}\text{O}_{49}$ can be excited, and the photogenerated holes can reaction with H_2O or OH^- to generated $\cdot\text{OH}$. The “hot electrons” would generate by the LSPR effect owing to the existence of oxygen vacancies. The E_{CB} of $\text{W}_{18}\text{O}_{49}$ was not more negative than the $\text{O}_2/\cdot\text{O}_2^-$ potential (ca. -0.33 eV), so the “hot electrons” would be injected into the E_{CB} of $\text{g-C}_3\text{N}_4$ and react with the dissolved oxygen to generate $\cdot\text{O}_2^-$. This phenomenon contributed to the enhanced photocatalytic activity of the prepared $\text{W}_{18}\text{O}_{49}/\text{g-C}_3\text{N}_4$ nanograss composites under NIR light irradiation.

In a word, the dual-channel charge-carrier transfer path based on Z-scheme charge-carriers transfer behavior of semiconductor heterojunction and the metallic LSPR-induced “hot electrons” injection process results in the high photocatalytic performance of the binary $\text{W}_{18}\text{O}_{49}/\text{g-C}_3\text{N}_4$ nanograss composites, and the unique nanograss structure further improve the light utilization efficiency of the prepared

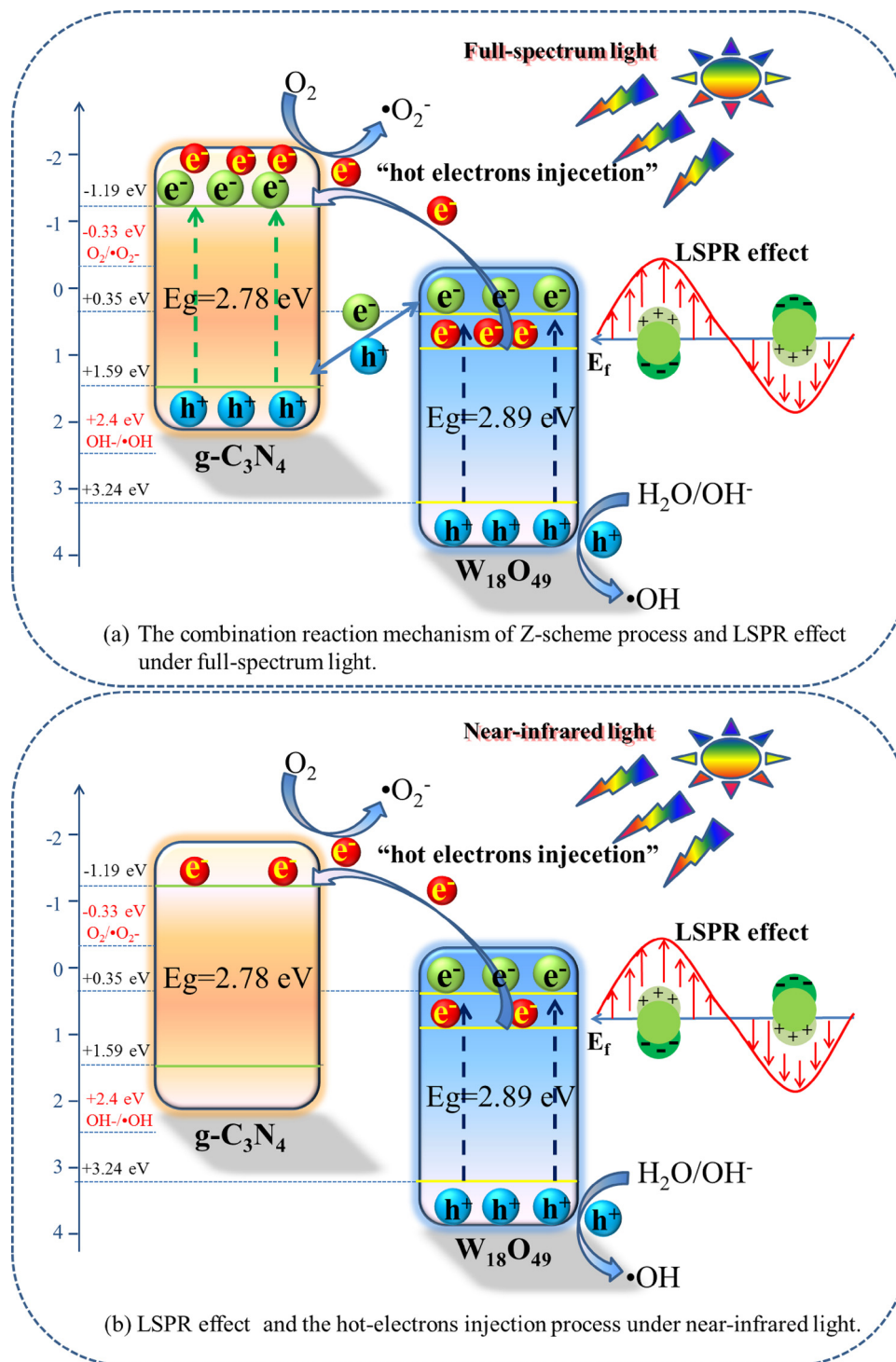


Fig. 13. Schematic illustration of the proposed reaction mechanism based on $W_{18}O_{49}/g-C_3N_4$ nanograss composite under (a) full-spectrum light ($\lambda > 365$ nm) and (b) NIR light irradiation ($\lambda > 700$ nm).

$W_{18}O_{49}/g-C_3N_4$ hybrid composites. The three main advantages of the $W_{18}O_{49}/g-C_3N_4$ nanograss composites bring about the greatly promoted photogenerated electrons and holes transfer rate, and realize a highly efficient full-spectrum-driven photocatalyst.

4. Conclusion

In conclusion, novel Z-scheme $W_{18}O_{49}/g-C_3N_4$ nanograss composites have been successfully synthesized via the hierarchical assembly of nonstoichiometric tungsten oxide ($W_{18}O_{49}$) onto the surface of $g-C_3N_4$

nanosheets. The prepared $W_{18}O_{49}/g-C_3N_4$ nanograss composites present high photocatalytic activity under both full-spectrum and NIR light irradiation, and show highly removal efficiency for both colorful MB and colorless CIP. The boosted photocatalytic activity of the prepared $W_{18}O_{49}/g-C_3N_4$ nanograss composites originates from the unique dual-channel charge-carrier transfer path: Z-scheme-improved charge-carriers separation and plasmon-induced "hot electrons" injection process. The unique nanograss structure can bring about more light reflection and refraction process, which improve the utilization of light energy. Control experiments demonstrated that the oxygen vacancies influence

the photocatalytic activity of $W_{18}O_{49}/g-C_3N_4$ nanograin composites greatly. Our work provide a new insight into the combination of the outstanding electrons property of nonmetal plasmonic and the highly efficient charge transfer Z-scheme reaction mechanism for the design and develop of highly efficient photocatalysts, and promoting the development of the next generation of low-cost highly efficient Z-scheme photocatalysts for future contaminants removal and environmental remediation.

Acknowledgments

The study was financially supported by Projects 51579096, 51521006, 51222805, 51409024 and 51709103 supported by National Natural Science Foundation of China, the Key Research and Development Program of Hunan Province of China (2017SK2241), and the National Program for Support of Top-Notch Young Professionals of China (2012).

Appendix A. Supplementary data

Supplementary material related to this article can be found, in the online version, at doi:<https://doi.org/10.1016/j.apcatb.2018.04.075>.

References

- [1] H. Wang, L. Zhang, Z. Chen, J. Hu, S. Li, Z. Wang, J. Liu, X. Wang, *Chem. Soc. Rev.* 43 (2014) 5234–5244.
- [2] M. Zhang, W. Luo, Z. Wei, W. Jiang, D. Liu, Y. Zhu, *Appl. Catal. B: Environ.* 194 (2016) 105–110.
- [3] J.J. Wang, L. Tang, G.M. Zeng, Y.C. Deng, Y.N. Liu, L.L. Wang, Y.Y. Zhou, Z. Guo, J.J. Wang, C. Zhang, *Appl. Catal. B: Environ.* 209 (2017) 285–294.
- [4] L. Tang, J.J. Wang, G.M. Zeng, Y.N. Liu, Y.C. Deng, Y.Y. Zhou, J. Tang, J.J. Wang, Z. Guo, *J. Hazard. Mater.* 306 (2015) 295–304.
- [5] Q. Wang, W. Wang, L. Zhong, D. Liu, X. Cao, F. Cui, *Appl. Catal. B: Environ.* 220 (2018) 290–302.
- [6] J. Yang, D. Chen, Y. Zhu, Y. Zhang, Y. Zhu, *Appl. Catal. B-Environ.* 205 (2017) 228–237.
- [7] J. Li, L. Cai, J. Shang, Y. Yu, L. Zhang, *Adv. Mater.* 28 (2016) 4059–4064.
- [8] X. Li, Y. Sun, T. Xiong, G. Jiang, Y. Zhang, Z. Wu, F. Dong, *J. Catal.* 352 (2017) 102–112.
- [9] J.J. Wang, L. Tang, G.M. Zeng, Y.N. Liu, Y.Y. Zhou, Y.C. Deng, J.J. Wang, B. Peng, *ACS Sustain. Chem. Eng.* 5 (2017) 1062–1072.
- [10] X. Li, J. Yu, M. Jaroniec, *Chem. Soc. Rev.* 45 (2016) 2603–2636.
- [11] J. Low, J. Yu, M. Jaroniec, S. Wageh, A.A. Al-Ghamdi, *Adv. Mater.* (2017) 29.
- [12] P. Zhou, J. Yu, M. Jaroniec, *Adv. Mater.* 26 (2014) 4920–4935.
- [13] L. Tang, Y.C. Deng, G.M. Zeng, W. Hu, J.J. Wang, Y.Y. Zhou, J.J. Wang, J. Tang, W. Fang, *J. Alloys Compd.* 662 (2016) 516–527.
- [14] J. Low, C. Jiang, B. Cheng, S. Wageh, A.A. Al-Ghamdi, J. Yu, *Small Methods* 1 (2017) 1700080.
- [15] Y. Deng, L. Tang, G. Zeng, C. Feng, H. Dong, J. Wang, H. Feng, Y. Liu, Y. Zhou, Y. Pang, *Environ. Sci.: Nano* 4 (2017) 1494–1511.
- [16] Y. Deng, L. Tang, C. Feng, G. Zeng, J. Wang, Y. Zhou, Y. Liu, B. Peng, H. Feng, *J. Hazard. Mater.* 344 (2018) 758–769.
- [17] Y. Deng, L. Tang, C. Feng, G. Zeng, J. Wang, Y. Lu, Y. Liu, J. Yu, S. Chen, Y. Zhou, *ACS Appl. Mater. Interfaces* 9 (2017) 42816–42828.
- [18] Z. Zhang, A. Li, S.W. Cao, M. Bosman, S. Li, C. Xue, *Nanoscale* 6 (2014) 5217–5222.
- [19] Z. Lin, X. Wang, *Angew. Chem. Int. Ed.* 52 (2013) 1735–1738.
- [20] Y. Zheng, Y. Jiao, Y. Zhu, Q. Cai, A. Vasileff, L.H. Li, Y. Han, Y. Chen, S.Z. Qiao, *J. Am. Chem. Soc.* 139 (2017) 3336–3339.
- [21] X. Wang, X. Chen, A. Thomas, X. Fu, M. Antonietti, *Adv. Mater.* 21 (2009) 1609–1612.
- [22] D. Zheng, X.N. Cao, X. Wang, *Angew. Chem. Int. Ed.* 55 (2016) 11512–11516.
- [23] T. Xiong, W. Cen, Y. Zhang, F. Dong, *ACS Catal.* 6 (2016) 2462–2472.
- [24] J. Wang, L. Tang, G. Zeng, Y. Deng, H. Dong, Y. Liu, L. Wang, B. Peng, C. Zhang, F. Chen, *Appl. Catal. B: Environ.* 222 (2018) 115–123.
- [25] W. Yu, J. Chen, T. Shang, L. Chen, L. Gu, T. Peng, *Appl. Catal. B: Environ.* 219 (2017) 693–704.
- [26] D.J. Martin, P.J. Reardon, S.J. Moniz, J. Tang, *J. Am. Chem. Soc.* 136 (2014) 12568–12571.
- [27] Y.C. Deng, L. Tang, G.M. Zeng, J.J. Wang, Y.Y. Zhou, J.J. Wang, J. Tang, Y.N. Liu, B. Peng, F. Chen, *J. Mol. Catal. A: Chem.* 421 (2016) 209–221.
- [28] Z. Zhang, J. Huang, Y. Fang, M. Zhang, K. Liu, B. Dong, *Adv. Mater.* (2017) 29.
- [29] H. Tada, T. Mitsui, T. Kiyonaga, T. Akita, K. Tanaka, *Nat. Mater.* 5 (2006) 782–786.
- [30] Hyeon Jin Yun, Hyunjo Lee, Nam Dong Kim, David Minzae Lee, Yu Sungju, J. Yi, *ACS Nano* 5 (2011) 4084–4090.
- [31] M.M. Shahjamali, M. Salvador, M. Bosman, D.S. Ginger, C. Xue, *J. Phys. Chem. C* 118 (2014) 12459–12468.
- [32] Z. Lou, Q. Gu, L. Xu, Y. Liao, C. Xue, *Chem. Asian J.* 10 (2015) 1291–1294.
- [33] S. Wang, Y. Gao, Y. Qi, A. Li, F. Fan, C. Li, *J. Catal.* 354 (2017) 250–257.
- [34] I. Krieger, C. Jiang, J. Rodriguez-Fernandez, R.D. Schaller, D.V. Talapin, E. da Como, J. Feldmann, *J. Am. Chem. Soc.* 134 (2012) 1583–1590.
- [35] H. Cheng, T. Kamegawa, K. Mori, H. Yamashita, *Angew. Chem. Int. Ed.* 53 (2014) 2910–2914.
- [36] Masayuki Kanehara, Hayato Koike, Taizo Yoshinaga, T. Teranishi, *J. Am. Chem. Soc.* 131 (2009) 17736–17737.
- [37] J. Yan, T. Wang, G. Wu, W. Dai, N. Guan, L. Li, J. Gong, *Adv. Mater.* 27 (2015) 1580–1586.
- [38] M. Seifollahi Bazarjani, M. Hojamberdiev, K. Morita, G. Zhu, G. Cherkashinin, C. Fasel, T. Herrmann, H. Breitzke, A. Gurlo, R. Riedel, *J. Am. Chem. Soc.* 135 (2013) 4467–4475.
- [39] J. He, H. Liu, B. Xu, X. Wang, *Small* 11 (2015) 1144–1149.
- [40] G. Xi, S. Ouyang, P. Li, J. Ye, Q. Ma, N. Su, H. Bai, C. Wang, *Angew. Chem. Int. Ed.* 51 (2012) 2395–2399.
- [41] J. Liu, O. Margeat, W. Dachraoui, X. Liu, M. Fahlman, J. Ackermann, *Adv. Funct. Mater.* 24 (2014) 6029–6037.
- [42] Y.C. Deng, L. Tang, G.M. Zeng, Z.J. Zhu, M. Yan, Y.Y. Zhou, J.J. Wang, Y.N. Liu, J.J. Wang, *Appl. Catal. B: Environ.* 203 (2017) 343–354.
- [43] Alessandra Tocchetto, A. Glisenti, *Langmuir: ACS J. Surf. Colloids* 16 (2000) 6173–6182.
- [44] S.V. Chong, B. Ingham, J.L. Tallon, *Curr. Appl. Phys.* 4 (2004) 197–201.
- [45] Y.C. Deng, L. Tang, G.M. Zeng, J.J. Wang, Y.Y. Zhou, J.J. Wang, J. Tang, L.L. Wang, C.Y. Feng, *J. Colloid Interface Sci.* 509 (2018) 219–234.
- [46] Z. Zhang, J. Huang, M. Zhang, Q. Yuan, B. Dong, *Appl. Catal. B: Environ.* 163 (2015) 298–305.
- [47] Z. Zhang, K. Liu, Z. Feng, Y. Bao, B. Dong, *Sci. Rep.* 6 (2016) 19221.
- [48] C.H. Choi, L. Lin, S. Gim, S. Lee, H. Kim, X. Wang, W. Choi, *ACS Catal.* (2018) 4241–4256.
- [49] Y. Li, L. Fang, R. Jin, Y. Yang, X. Fang, Y. Xing, S. Song, *Nanoscale* 7 (2015) 758–764.
- [50] Y. Shang, X. Chen, W. Liu, P. Tan, H. Chen, L. Wu, C. Ma, X. Xiong, J. Pan, *Appl. Catal. B: Environ.* 204 (2017) 78–88.
- [51] S. Samanta, R. Srivastava, *Appl. Catal. B: Environ.* 218 (2017) 621–636.
- [52] X. Liu, Q. Zhang, G. Xing, Q. Xiong, T.C. Sum, *J. Phys. Chem. C* 117 (2013) 10716–10722.